Electrocatalysts for CO_2 reduction to multicarbon products beyond copper from systematic first principle-based screening

Georg Kastlunger*

Catalysis Theory Center, Department of Physics,
Technical University of Denmark (DTU), 2800 Kgs. Lyngby, Denmark

Utilizing electrochemical conversion of $CO_{(2)}$ into hydrocarbons is envisioned as a strategy towards closing the carbon cycle in an effort to reduce anthropogenic climate change. The process, however, suffers from low energy efficiency and selectivity towards tailored products. To this day, success in producing significant amounts of multicarbon products is limited to a single catalyst, copper.

In this paper, we present an *ab initio* screening study focusing on the discovery of Cu-free catalysts for the production of high value carbon products. In a sequential screening process, both intrinsic activity and catalyst stability have been investigated. This lead to the discovery of a series of alloys containing transition and post transition metals exhibiting promising activity together with stability against segregation. Selectivity against hydrogen production and oxidation tendencies are also screened, highlighting the need for caution regarding the latter at non-reducing conditions.

Electronic structure arguments are provided rationalizing the performance of the selected catalysts, which can be applied as guiding principles for the discovery of novel alloy catalysts for the reaction. Based on this fundamental understanding, this work motivates experimental testing of predicted catalyst compositions and provides an intuitive rational for the prediction of further catalyst candidates.

INTRODUCTION

Electrochemical reduction of carbon dioxide (eCO_2R) represents one of the most direct strategies to achieve independence from fossil carbon sources.[1] By converting CO_2 into energy-rich hydrocarbons using renewable electricity, this approach not only mitigates greenhouse gas emissions but also enables the sustainable synthesis of fuels and chemicals. [2] In principle, the standard reduction potentials towards the plethora of accessible hydrocarbons and oxygenates promise efficient and reliable conversion, with the most desired products, ethylene, ethanol & propanol even exhibiting more positive values than the hydrogen evolution reaction (HER). [3] However, the reactions to the highlighted products are sluggish, creating an unavoidable competition with HER, which disqualifies nearly all common electrocatalysts for the processes. [4]

Today, copper (Cu) remains the benchmark catalyst for eCO_2R, uniquely capable of producing multi-carbon (C_{2+}) products in significant amounts. [5, 6] However, its moderate selectivity and susceptibility to surface restructuring motivate the search for alternative materials. [7] Computational screening is a powerful tool in this endeavor, enabling the rapid evaluation of alloy compositions, surface energetics, and adsorption properties. Several screening attempts have been made towards the identification of alternative catalysts in eCO_2R.

In 2016, Hansen et al screened bimetallic alloys for methane production. [8]. They found that several alloys might be able to reduce the overpotential relative to copper but highlighted their low stability against corrosion at reaction

https://doi.org/10.26434/chemrxiv-2025-b865s-v2 **ORCID:** https://orcid.org/0000-0002-3767-8734

conditions.

Similarly, Abild-Pedersen and collaborators have conducted systematic DFT screening of binary alloys in cubic $L1_2$ and $L1_0$ geometries based on CO* (* denotes a surface bond) and C* formation energies as descriptors for C_{2+}activity and selectivity.[9] Their work highlighted the role of p-block elements in tuning adsorption energetics and again emphasized the importance of alloy stability under reaction conditions.

Ulissi and co-workers pioneered the use of active learning and machine learning-guided DFT screening to navigate vast intermetallic spaces, identifying promising surfaces for both $eCO_2R$and hydrogen evolution using the classical descriptors of CO* and H* formation energies. [10] Their work demonstrated that data-driven approaches can accelerate the identification of viable electrocatalysts across diverse chemical families. One of the most relevant predictions, CuAl, was later shown to in fact outperform bare Cu's activity [11].

The identification of copper-free catalysts would be of particular interest as they would on one side avoid false positive experimental testings, where the copper alone is responsible for activity [12] and further might be able to avoid some copper's shortcomings. The limited success in the identification of relevant Cu electrocatalysts of the mentioned and additional screening studies can likely be attributed to eCO_2R's clear kinetically controlled mechanisms, [13] necessitating the study of reaction barriers, and the fact that incorporating metastable intermediates is key. Particularly, the latter is essential when screening for multicarbon products, where the majority of theoretical and experimental studies agree that the dimerization of two adsorbed CO molecules into a strongly polarized adsorbate (*OCCO) is the rate-limiting step (RLS) towards all bi-carbon products. [14–16] *OCCO can, in principle, be stabilized in neutral gas-phase DFT calculations, as has first been achieved in 2013. [17] However, it relaxed into an unfavourable monodentate binding configuration. A thermodynamically much more stable intermediate can be stabilized if the reaction conditions are incorporated into simulations. [18] For example, incorporating a solvation shell can already suffice to stabilize this favourable conformer [19]. Further, incorporating the electrode potential, by means of a surface charge on the catalyst, is also a straightforward method for accessing this key intermediate towards multicarbon products. [14, 20] Stepping towards such a methodology, Wang et al recently identified the same enhancement of Cu's activity by adding Al as Tran et al. However, they did not venture beyond Cu-containing alloys. [20]

Building on the foundations of previous studies, here we apply a sequential ab-initio screening strategy to identify (Cu-free) alloy catalysts for eCO_2R. In this workflow, we filter bimetallic catalysts including late and post transition metals, whose convex hulls and crystal symmetries have been retrieved from the Material project database [21], followed by evaluating their activity, stability, and selectivity via individual descriptors. This allowed us to unravel and rationalize systematic eCO_2R catalyst design principles for bimetallic alloys. We show that among the late transition metals (TM) Pd is generally most succeptible to ligand effects, moving its d-band close to Cu's, while no alloys with Ir and Rh could be identified that weaken the CO-affinity enough. The magnitude of the effect of the ligand on the TMs depends greatly on the alloying partner, where we highlight promising elemental composition ratios for varying combinations of noble metals and post transitions metals (PTM).

Overall, our screening hopefully motivates the experimental evaluation of the proposed electrocatalysts. Ideally, it would lead to the discovery of catalysts that could produce specific eCO_2Rproducts in a more selective fashion and experimental lifetimes beyond Cu's. Further, our screening allows for a glimpse into the fascinating world of d-band manipulation via PTM alloying and shows the possibility of varying specific descriptor values by means of geometric and compositional aspects of the applied alloys.

SCREENING STRATEGY

Initial alloy selection

As a starting point, the materials project database [21] was parsed for existing alloys containing combinations of late transition metals and the post transition metals Zn, Ga, Ge, Cd, In, Sn, Sb, Hg, Pb, Bi. The initial criteria for the query were (i) The alloy lies on the convex hull (ii) The alloy has at least one entry in the ICSD database (iii) The alloy has no bandgap (iv) The number of atoms in the unit cell does not exceed 10 atoms.

Once an alloy passed the above query, it was chosen as a possible candidate, and the crystal bulk was relaxed in terms of both the atomic positions and unit cell size (ISIF=3). Then, the following surface specific parameters were screened.

Surface energy

After relaxation, the bulk crystals were cut to create their respective surfaces by applying the CatKit software.[22] In order to determine the alloy's surface facets with lowest surface energy, slabs of a minimum thickness of 10Å were created. The slabs were relaxed below a maximum force threshold of 0.03eV/Å. Then the surface energy was calculated as [23]

$$\epsilon_{surf} = \frac{E_{slab} - \frac{N_{a,slab}}{N_{a,bulk}} E_{bulk}}{2A_{slab}}, \tag{1}$$

where E_{slab} and E_{bulk} correspond to the potential energies of the relaxed slab and the bulk unit cell, $N_{a,slab}$ and $N_{a,bulk}$ represent the number of atoms in the slab and bulk system, respectively, and A_{slab} is the surface area of the created slab. Two aspects need to be considered with care for calculating meaningful surface energies for the alloys. First, the created slab needs to exhibit the same stoichometry as the bulk unit cell, and second, the two surfaces of the created slab need to mirror each other. In order to ensure both criteria are satisfied, slabs of gradually increasing thickness were created and checked for their composition and surface geometries until symmetric slabs of correct composition were created, which were then relaxed. Miller indices up to 2 were regarded, where for trigonal and hexagonal structures values from -2 to 2 were chosen. Patterns in the most stable surfaces were found throughout the alloys, where the specific Miller indices govern for given space groups. The most stable surfaces for the varying space groups are summarized in table I. The mentioned facets were chosen for further analysis if not mentioned otherwise.

Lattice (Colors will be used for alloys labels)	Investigated facets for given Space groups (colors will be used for markers in figures)		
Cubic	Pm-3m: 111, 100, 110	Fm-3m: 110 , 100	
Tetragonal	P4/mmm: 110, 100	I4/mmm: 112, 100,	
Hexagonal	$P6_3$/mmc: 11-20, 2-1-10, 0001	P-62m: 0001	P6/mmm: 0001,11-20
Orthorhombic	Pnnm: 101, 001	Pnma: 010	Cmmm: 021, 100 (3/1 ratio), 221, 001 (5/3 ratio)
Trigonal	R-3m: 0001, 1-102	P-3m1: 11-20,2-1-10	

TABLE I. Identified most stable facets for the varying screened crystal structures. The facets have been sorted with reducing stability. Note that only facets which could exhibit a mirror symmetry in the slab have been regarded as only in such a case the surface energies are meaningful.

CO binding free energy

Up to three most stable facets were applied in the determination of the binding free energy of CO ($\Delta G_{*\mathrm{CO}}$). Here, all symmetrically unique binding sites on the respective alloy surface were sampled applying the adsorption site finder of CatKit.[22] The surface plane area varied based on the crystal structure, but was composed of at least 9 surface atoms. A minimal slab thickness of 4 atomic layers was used. The lowest two metal layers were constrained in the bulk positions.

The most stable binding site on each element of the alloy was chosen for the analysis. The site's "element" noted in upcoming figures is defined as the atom closest to the carbon atom and different coordinations were treated equally. The rational for choosing only the most stable site was that these sites would be covered first, possibly denying access to and likely changing the binding properties on the weaker binding sites.

$\Delta G_{*\mathrm{CO}}$was calculated as

$$\Delta G_{*\mathrm{CO}} = G_{*\mathrm{CO}} - G_{*} - G^{o}_{\mathrm{CO,g}}, \tag{2}$$

where G_{CO} and G_{*} represent the Gibbs free energy of the slab with adsorbed CO (*CO) and the empty slab (*), respectively, after their relaxation below a force threshold of 0.03eV/Å. $G^{o}_{CO,g}$ is the standard free energy of CO in gas phase (T=298K, p=1bar). Refer to the computational details for further details on their definition.

After determining the CO binding properties, alloys exhibiting -0.75eV $<$ $\Delta G_{*\mathrm{CO}}$$<$ +0.2eV were chosen to progress to the calculation of surface segregation energies.

Segregation energy

Segregation in vacuum

Surface segregation tendencies were estimated by exchanging an atom of each element in the bulk (4th layer) of the slab with an atom of the other species on the surface. In order to guarantee a dillute limit in these calculations and to approximate bulk behaviour, the slab sizes in this study were chosen to consist of at least 12 atoms in the surface plane and 6 atomic layers in the perpendicular directions. The positions of the atoms in the lowest layer of the slab were constrained. Finally, the surface segregation energy of a species i was calculated as

$$\Delta E^{vac}_{seg,i} = E^{vac}_{exch,i} - E^{vac}_{0}, \tag{3}$$

where $E_{exch,i}$ refers to the potential energy of the slab where atom i in the bulk was exchanged with another atom of differing species on the surface and E^{vac}_0 is the reference energy derived from the unsegregated alloy.

Segregation in a CO atmosphere

In order to judge about segregation of the alloy's components at reaction conditions, we also approximated the segregation energies including CO binding on the surface. A simplified approach which allows the estimation from already existing data was chosen, allowing an efficient and streamlined stability judgements. Here, the segregation energy is determined by extending the segregation energy in equation 3 by the difference in the most stable $\Delta G_{*\mathrm{CO}}$on the respective elements on the unsegregated surface (determined in). Hence, the segregation of an atom species i in a CO atmosphere has been approximated as

$$\Delta E^{CO}_{seg,i} = \Delta E^{vac}_{seg,i} + \Delta G_{*\mathrm{CO},j} - \Delta G_{*\mathrm{CO},i}, \tag{4}$$

where, $\Delta G_{*\mathrm{CO},i}$ and $\Delta G_{*\mathrm{CO},j}$ refer to the most stable unsegregated adsorption free energy of CO on the element whose surface segregation is probed (i) and the other element in the alloys (j) both in the unsegregated situation.

Catalysts that were identified to exhibit positive $\Delta E^{vac}_{seg,i}$ and $\Delta E^{CO}_{seg,i}$ for all elements of the alloy were chosen to progress to the next stage, i.e. the estimation of oxidation tendencies and the competition with the hydrogen evolution reaction.

Hydrogen evolution tendency and Oxophilicity

We conducted a simple test for estimating surface oxidation and hyrdogen evolution (HER) activity, by means of *OH and *H formation free energies, $\Delta G_{*\mathrm{OH}}$and $\Delta G_{*\mathrm{H}}$, defined as

$$\Delta G_{*\mathrm{OH}} = G_{*\mathrm{OH}} - G_{*} - G^{o}_{\mathrm{H_2O,l}} + \frac{1}{2} G^{o}_{\mathrm{H_2,g}} \tag{5}$$

and

$$\Delta G_{*\mathrm{H}} = G_{*\mathrm{H}} - G_{*} - \frac{1}{2} G^{o}_{\mathrm{H_2,g}} \tag{6}$$

where $G^{o}_{\mathrm{H_2O,l}}$ and $G^{o}_{\mathrm{H_2,g}}$ represent the standard free energies of liquid water (T=298K and p=0.032bar) and gaseous H_2 (T=298K and p=1bar).

As a strict exclusion criterion, a viable eCO_2Rcatalyst would not be *OH covered at reaction conditions (¡-0.5V_{RHE}), meaning ΔG_{*OH}should strictly be above -0.5eV. However, even a OH coverage at open circuit conditions would lead to corrosion of the catalyst and should thus ideally be avoided.

We note that we did not rigorously exclude the alloys that failed this text from the activity tests, as the oxidation tendency could possibly be circumvented by protecting the catalyst from exposure to the electrolyte until working potentials are set up.

Prominently, the ideal value of $\Delta G_{*H}$for HER has been identified as 0eV.[24] Further, if ΔG_{*H}becomes even more negative one could expect that a hydrogen monolayer would start to form, impeding eCO_2R. Based on these two arguments, we defined the criterion as ΔG_{*H}¿ 0eV.

Activity estimation

As the final criterion for promising catalyst candidates, we evaluated the remaining alloys on the simplified activity volcano of figure 1. Same as in figure 1, in this evaluation, we included $\Delta G_{*CO}$from a calculation in an uncharged slab-vacuum interface. The calculation of *OCCO's formation energy, defined as

$$\Delta G_{*\mathrm{OCCO}} = G_{*\mathrm{OCCO}} - G_{*} - 2G^{o}_{\mathrm{CO,g}}, \tag{7}$$

is not as simple, as the *OCCO spontaneously dissociates in such an interface. Thus, for calculating ΔG_{*OCCO}, we applied VASPSol [25], where we probed the state of adsorbed OCCO (*OCCO) and * at varying surface charges and determined energy vs potential curves from it, as described in more detail in the computational details.

RESULTS AND DISCUSSION

eCOR activity descriptors towards C2+ products

In order to justify the ΔG_{*CO} criterion for ideal activity, we will first discuss what defines the ideal eCO_2R catalyst. As is well established, CO is an early intermediate from CO_2 to all $>2e^-$ products. [3] Further, if evaluated on the SHE scale both CO_2 and CO reduction lead to comparable partial current densities towards C_2+ products [3, 14, 15], strongly suggesting that the rate limiting step (RLS) towards multicarbon products is located after producing CO. Early in the research on eCO_2R, Cu has been identified as the only viable catalyst, [26] which was later attributed to its ideal binding strength for CO and H, with the former being slightly exergonic and the latter being slighlty endergonic. [4] This combination of binding properties allows to create a coverage of *CO on the catalyst surface, while the hydrogen evolution is inhibited and no H-coverage is expected.

We would like to build upon this first assessment, adding means for activity estimation to the previous product selectivity maps. Figure 1 shows a simplified activity volcano calculated at a potential of -1 V vs SHE (V_{SHE}), where $\Delta G_{*OCCO}$and ΔG_{*CO}on the (100)-facets of common transition metals and their scaling line are shown explicitly. As is evident, Cu is located slightly to the left of the line denoting thermoneutrality for CO-adsorption. On the other

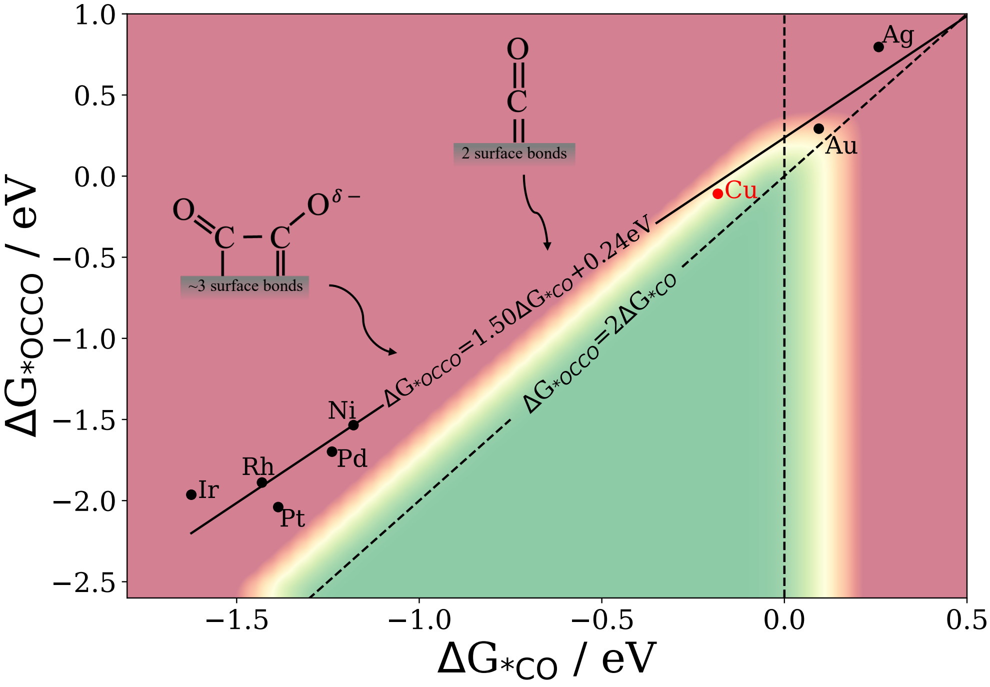

FIG. 1. Schematic CO_2 reduction activity plot towards C_{2+} products at -1V against the standard hydrogen electrode assuming *CO dimerization as the rate limiting step. The scaling line of the (100)-facet of the late transition metals is shown as a solid line. The dashed lines represent the lines of thermoneutrality of the RLS (diagonal dashed black line) and CO desorption (vertical dashed line at ΔG_{*CO}=0)

hand, Au and Ag, suffer from miniscule CO coverages, due to $\Delta G_{*\mathrm{CO}}$>0. The Pt-group metals, Ir and Rh tend to bind CO very strongly with $\Delta G_{*\mathrm{CO}}$<-1eV. We argue, that the strong binding strength of *CO alone does not justify the rejection of these strong binding elements as eCO_2R catalysts. Their failure, besides their tendency for HER [24], is rooted in the scaling line shown in figure 1. Two *CO species are necessary for creating *OCCO. Thus a scaling line between *CO and *OCCO with a slope below 2 automatically leads to a penalty in activity with increasing CO binding strength. This is the case in the scaling line shown in figure 1, which exhibits a slope of 1.5, as a consequence of the reduction in C-* bonds when changing from 2*CO to *OCCO. From this assessment, we can conclude that the ideal catalyst for eCO_2Rproducts being limited by *CO dimerization, a weak but still negative $\Delta G_{*\mathrm{CO}}$is desired and too negative $\Delta G_{*\mathrm{CO}}$leads to *CO poisoning over eCO_2Rbecause of an increase in activation energy of 0.5 times the reduction in $\Delta G_{*\mathrm{CO}}$.

Alloy selection based on CO binding strength

Figure 2 shows a subset of the screened CO binding energies exhibiting -0.75<$\Delta G_{*\mathrm{CO}}$<0.2. From the 23 originally screened transition metal (TM) alloys, eight have been identified as relevant based on this descriptor, where only two are copper free, namely AgPd and $AuPd_3$. Generally, TM alloys consisting of combinations among Pt- and

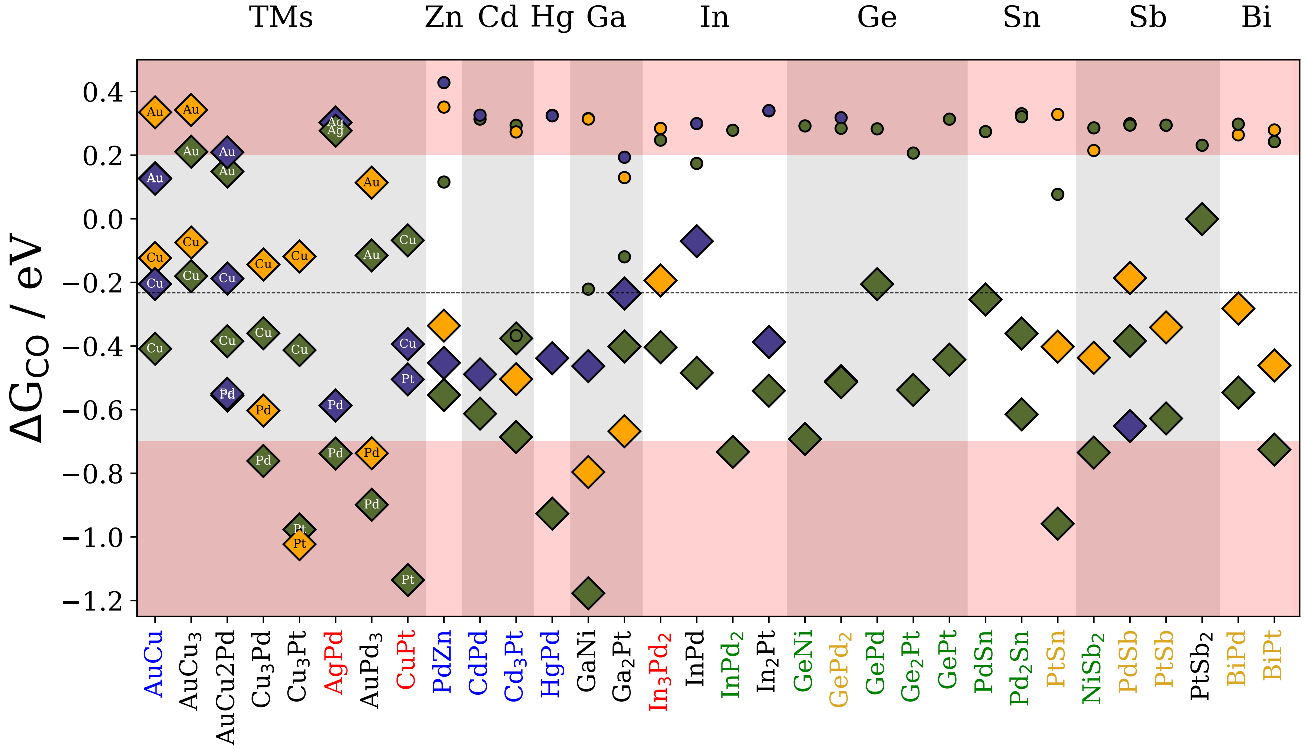

FIG. 2. Calculated CO adsorption free energies as defined in Eq. 2 of the selection of alloys passing the first criterion (-0.75eV$<\Delta G_{*\mathrm{CO}}<$0.2eV). A complete picture of all investigated alloys is given in figures S1-S2. Note that the color of the alloy label indicates the crystal structure, while the color of the markers indicate the facet, as described in table I. Further, diamonds refer to TMs sites, while the small circles represent the PTM sites. For pure TMs, the binding site identity is included in the diamonds explicitly. $\Delta G_{*\mathrm{CO}}$on Cu(100) is shown as a horizontal dashed line.

Ir-group metals, as well as their mixture tend to overbind CO, thus disqualifying as viable catalyst for eCOR. Similarly, combinations of Ag and Au underbind CO, thus not leading to a significant CO coverage crucial for $\mathrm{eCO_2R}$. Interestingly, alloys including Cu show promise, as the binding of CO on their Cu-sites is not altered significantly compared to pure Cu.

Combining Ag and Au with Pd, respectively, lead to promising candidates. In the former case, AgPd, the binding of CO on Pd sites is weakened substantially shifting it into the CO binding range of interest. In the case of $\mathrm{AuPd_3}$, on the other hand, the binding of CO on the Au sites is improved as a consequence of the slight upshift of Au's d-band center, allowing a significant CO coverage on these sites.

Screening the combination of late TMs and post-transition metals (PTM) lead to the identification of 24 promising candidates, shown in figure 2. In general, the influence of alloying on the CO binding strength on PTM sites, marked as little dots in figure 2, is minute and in most cases CO desorbs spontaneously from them or migrates to the stronger binding coinage metal sites with the only exception of Ga. Thus, their participation in $\mathrm{eCO_2R}$ could only consist of transforming $\mathrm{CO_2}$ into CO, creating an increased CO partial pressure close to the electrode analogoes to CuAg tandem catalysts. [27] Ga, on the other hand, exhibited an interesting downshift in $\Delta G_{*\mathrm{CO}}$, present on GaNi, $\mathrm{Ga_2Pt}$, GaIr and GaRh (see figure S2 for the latter two). Thus, Ga sites might be the only PTM sites relvant for eCO_2R.

In contrast, TMs experience a consistent downshift of in d-band center (see SI Figure S3) from alloying with PTMs. As a consequence, the binding strength of CO onPt-group metals is reduced considerably, shifting it into the region of interest on the alloys shown in figure 2. For coinage metals, the downshift in the d-band center has the opposite effect further inceasing $\Delta G_{*\mathrm{CO}}$on Au and Ag alloys and a priori disqualifying them as viable candidates. As the other extreme, the downshift of the d-band center does not suffice to reduce the CO binding strength on Rh and Ir enough for it to be of interest. This leaves only alloys of Pt-group metals and PTMs exhibiting the desired CO binding strength comparable to Cu-surfaces.

Among the Pt-group alloys, Pd showed the strongest response to alloying, where 12 alloys passed this criterion, with at least one candidate combination with all studied PTMs, all three Pd:PTM combinations of 1:1, 1:2, 2:1 compositions have been identified as viable. Pt alloys exhibit the second strongest ligand effect among the Pt-group metals, 9 viable candidates for eCO_2Rhave been identified. The Pt content in the identified candidates is lower than for Pd including Pt:PTM combinations of 1:1, 1:2 and 1:3. Finally, Ni is the least responsive element within the Pt-group, where only 3 viable alloys have been identified consisting of GaNi, GeNi and $NiSb_2$.

Among the studied PTMs the ligand effect increased from group 12 metals towards the right of the periodic table. This leads to 1:! combinations of Pd with Zn and Cd being promising candidates, while Ni and Pt would still overbind CO when alloyed with the two. The ligand effect arising from alloys with the p-block elements was found to be comparable among all Pt-group metals. In summary, several design principles for alloys viable in eCO_2R could be identified in this first test, being: (i) Alloys of Pt,Pd and Ni and post-transition metals approach CO binding strengths close to Cu as a consequence of the downshift in the noble metal d-band center. (ii) The ligand effect leading to this downshift experienced by the Pt-group metals follows the order Pd > Pt > Ni. (iii) Zn and Cd create significantly lower ligand effects than the p-block elements. (iv) Ga, interestingly, can be activated for the reaction by alloying with noble metals.

SURFACE STABILITY

After substantally reducing the number of relevant alloys based on their CO-binding affinity, we probed their surface stability. Figure3, shows the computed segregation energies in a vacuum (top) and a CO gas interface (bottom), as defined in section . We found that $\Delta E_{seg}^{vac}$for alloys consisting of only TMs does not exceed a value of 1eV/atom, which we attribute to their weak formation free energy ranging only between 0 and -0.18eV/atom for the TM alloys in Figure 3. [21] As a further consequence of the low formation energies, Au and Ag tend to cover the surface of alloys containing them due to their comparatively low surface energies, i.e. 44 meV/Å and 48 meV/Å for their (111)-surfaces respectively. [28] The remaining alloys of Cu with Pt and Pd are stable against segragation in vacuum as they exhibit slightly more negative formation energies and the two elements' comparable surface energies, i.e. 84, 93 and 85 meV/Å for the (111)-facet of Cu, Pt and Pd, respectively. [28]

When a transition metal is alloyed with a post transition metal, ΔE_{seg}^{vac} can reach up to nearly 4eV. We attribute this to the more substantial formation energies of the TM-PTM alloys, reaching well below -0.5 eV/atom, and the

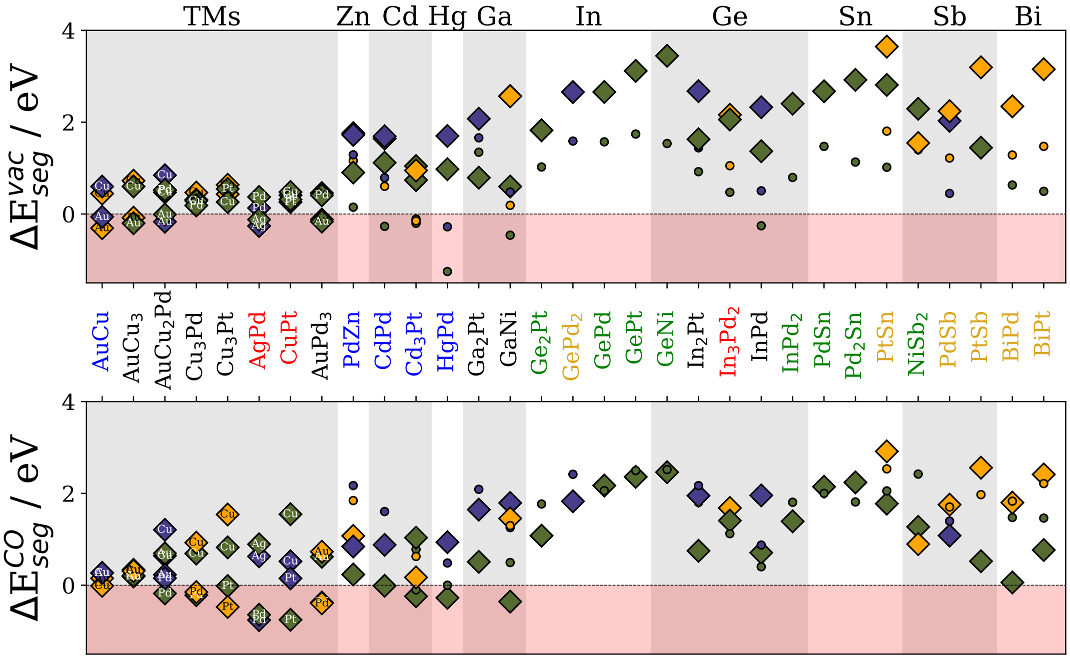

FIG. 3. Segregation energies in vacuum and in a CO-atmosphere for the surface segregation of the respective elements included in the alloys exhibiting promising $\Delta G_{*\mathrm{CO}}$. The color of the alloy label indicates the crystal structure, while the color of the markers indicate the facet, as described in Table I. Diamonds refer to TMs sites, while the small circles represent the PTM sites. For pure TM-alloys, the segregating element is included in the diamonds explicitly. Negative values represent a tendency of the respective element to segregate on the alloy surface, thus destroying the alloy structure and deviating from the $\Delta G_{*\mathrm{CO}}$ shown in figure 2

.

difference in atomic radii which leads to substantial distortion in the lattice upon element exchange. In general, all PTMs exhibit a lower ΔE_{seg}^{vac} than their TM counterparts, as a consequence of their lower surface energies. [28] In some cases, particularly when Cd and Hg are involved this trend leads to instability of the alloys due to surface segregation of the PTMs.

Interestingly, ΔE_{seg}^{vac} and ΔE_{seg}^{CO} nearly mirror each other. Although low surface energy elements such as Au, Ag and the PTMs have higher tendency to migrate to the surface in vacuum, once *CO is present, their alloying element would rather cover the surface. This is a consequence of the substantially larger CO binding strength on the noble metals compared to the other elements contained in figure 3b, as can be seen in figure 2, where CO even spontaneously desorbed from the PTM sites.

This analysis disqualified all the pure TM composites, with only AuCu$_x$ showing promise to be stable at reaction conditions but not in a vacuum environment. Note that the analysis in principle also disqualified GaNi. We, however, keep the alloy given the experimental finding that Ni-Ga alloys are able to produce multicarbon products in eCO$_2$R. [29]

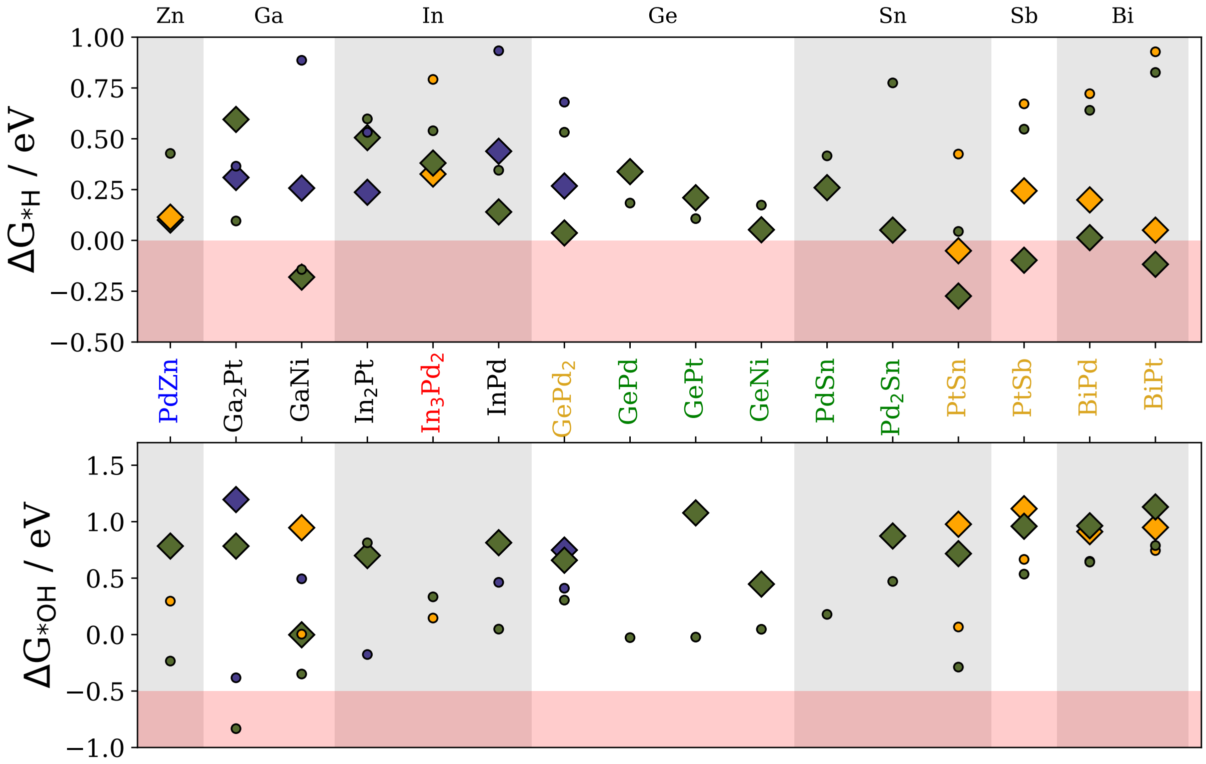

FIG. 4. Formation free energies of *H and *OH from water at $0\mathrm{V}_{\mathrm{RHE}}$ on the remaining candidates. Colors correspond to the patterns outlined in Table 1. Diamonds represent the TM sites, while circles denote the PTM sites. Only the most stable binding sites on the respective alloys and elements are shown.

OXIDATION RESISTANCE AND HER TENDENCY

Figure 4 shows both the formation energies of *H (top) and *OH (bottom) from water at 0V vs RHE ($\mathrm{V}_{\mathrm{RHE}}$) on the again reduced set of alloys. Generally, the TM's exhibit an increased hydrogen affinity. This is consistent with their stronger affinity for CO, as $\Delta G_{*\mathrm{CO}}$and $\Delta G_{*\mathrm{H}}$scale. [4] $\Delta G_{*\mathrm{H}}$on the hexagonal alloys of Pt with Sn, Sb and Bi and NiGa exhibited facets where $\Delta G_{*\mathrm{H}}$falls below the selectivity criterion of 0. With the exception of PtSn, all of these alloys, however, show a positive $\Delta G_{*\mathrm{H}}$on their most stable facets, which is why we did not exclude them for the following step. All other alloys satisfy the selectivity criterion but approach the ideal value for HER activity ($\Delta G_{*\mathrm{H}}$=0) in come cases. Here, Pd alloys generally show higher promise with more positive $\Delta G_{*\mathrm{H}}$'s than Pt and Ni alloys. This can be attributed to Pd's overall stronger reaction to ligands as has already been discussed in the context of the $\Delta G_{*\mathrm{CO}}$criterion.

Figure 4b shows that PTMs exhibit stronger oxidation tendencies throughout than the TMs, with their OH-affinity falling below $\Delta G_{*\mathrm{OH}}$=0 in several cases, meaning that the surfaces are covered by *OH at $0\mathrm{V}_{\mathrm{RHE}}$. As an exclusion criterion in this analysis, we chose the somewhat arbitrary value of $\Delta G_{*\mathrm{OH}}$¡-0.5eV with the rational that lowest overpotentials for $\mathrm{eCO_2R}$ to C_{2+} have been reported below -0.5$\mathrm{V}_{\mathrm{RHE}}$. Thus, we judge whether surfaces are covered by *OH at reaction conditions. [30] Note that oxidation upon air and electrolyte exposure might occur nonetheless, which demands great care. [31, 32] In a few cases, such as for $\mathrm{In_3Pd_2}$, GePd, PdSn no stable geometries could be

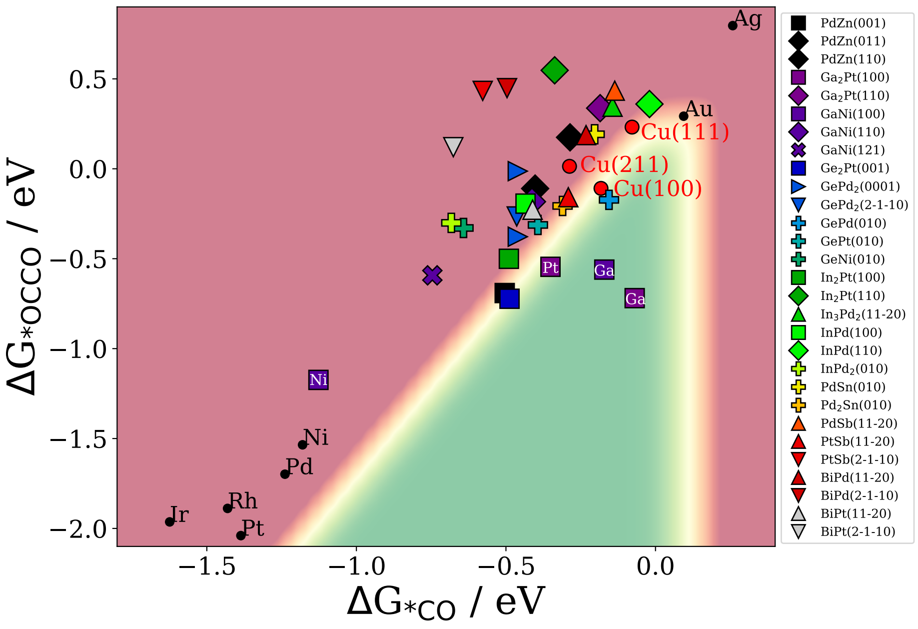

FIG. 5. Activity plot for eCO_2R to multicarbon products at -1V_{SHE} containing the alloys that showed promising characteristics in the previous tests. Note that in the 100-facets of NiGa and Ga_2Pt both the TMs and Ga-covered surfaces have been considered and the element covering the surface has been explicitly noted.

identified, where the OH would not spontaneously migrate from the TM to the PTM in geometry optimizations.

The studied Ga-containing alloys exhibited the highest oxidation tendencies followed by PtSn, PdZn and In_2Pt with at least one facet with $\Delta G_{*\mathrm{OH}}$¡0. On the other hand the highest stability against oxidation could be identified for alloys containing Sb and Bi. For Bi, this we attribute to the large radius of the element enhaning Pauli repulsion in *OH-formation. [33] For Sb, the rational is not as clear cut.

Overall, we found that increasing the TM content helps the overall oxidation stability ($\Delta G_{*\mathrm{OH}}$ of PTM sites increases), but also increases the HER tendency ($\Delta G_{*\mathrm{H}}$ of TM sites reduces). We show this in more detail in SI figure S4, based on the example of Pd-Sn alloys.

ACTIVITY ESTIMATION

With this final selection of alloys, we estimated their eCO_2R activity based on Figure 1's volcano, which we show in Figure 5. Several promising candidates could be identified. Particularly, the Ga-sites of NiGa and Ga_2Pt, showed an extraordinary stabilization of *OCCO making them very ideal candidates. The most promising facet on the two catalysts correspond to their (100)-facets, where Ga forms a monolayer on the surface. As we show in figure S5, forming a monolayer of Ga or Zn on the fcc-metals does indeed lead to a remarkable stabilization of *OCCO. However, in most cases $\Delta G_{*\mathrm{CO}}$ is a little more positive than on Cu and their stability in electrochemical conditions should be evaluated.

In general, the (100)-facets of cubic alloys show the highest promise, as they tend to stabilize *OCCO compared to their more stable (111) or (110) surfaces for fcc and bcc-like crystals, respectively. Such a fourfold-site does not exist on hcp-surfaces, where we found that the most stable 11-20 surface is stabilizing *OCCO better than 2-1-10. Finally, orthorhombic surfaces orthorhombic surfaces, also show promise, particularly for GePd located very closely to Cu(100).

A more systematic comparison between cubic/tetragonal and hexagonal surfaces based on Pd- and Pt-alloys with all investigated post transition metals is shown in Figure S6. The comparison shows that hexagonal 1:1 alloys exhibit a smaller reduction in $\Delta G_{*\mathrm{CO}}$relative to the pure TMs than cubic and tetragonal alloys, suggesting a reduced ligand effect. Thus, Zn and Cd alloys overbind *CO on hexagonal crystal surfaces, while they bind comparable to Cu on the rectangular Pd-alloys. We note that the binding strength can be systematically increased though by increasing the share of the TM in the alloys and reduced by increasing the PTM amount, analogous to the results shown in figure S4.

On the other hand, the remaining PTMs bind CO close to ideally on hexagonal 1:1 alloys, while *CO binds too weakly on the cubic and tetragonal Pd-surfaces. Interestingly, tetragonal 1:1 Pt-PTM alloys containing Ga, Ge, Sn and In would exhibit both ideal $\Delta G_{*\mathrm{CO}}$and simultaneously stabilize *OCCO substantially more than Cu. Unfortunately, Pt-PTM alloys of such a composition generally favor other crystal structures. Forcing the alloys into this crystal structure might be fruitful approach to creating active catalysts for the reaction.

As a final note, we highlight that several of the predicted promising alloys have recently been characterized experimentally by Clark et al. following similar selection criteria in spirit but from an experimental perspective rather than simulations. [31] Although, measured descriptor quantities such as d-band centers, work functions, CO binding strengths clearly reflect the findings in our work, no $\mathrm{eCO_2R}$ activity measurements have been reported, which we strongly motivate. As also highlighted by Clark et al, we stress that tested alloys need to be treated with care, as several steps from synthesis to testing at working conditions might lead to surface oxidation of the catalysts, triggering reconstruction and dealloying.

CONCLUSIONS

In this work, we presented a first-principles-based screening study aimed at identifying alloy catalysts for $\mathrm{eCO_2R}$ to multicarbon products.

First, we highlighted how Cu's unique $\mathrm{eCO_2R}$ ability can be explained intuitively based on the scaling relation slope between $\Delta G_{*\mathrm{CO}}$ and $\Delta G_{*\mathrm{OCCO}}$, which reflects the reduction in C-surface bonds upon dimerization. This finding allowed us to define an activity volcano for activity screening.

Our screening protocol incorporated a sequence of computational filters based on $\Delta G_{*\mathrm{CO}}$, surface segregation energies in vacuum and under a CO atmosphere, oxidation resistance, and competition with the hydrogen evolution reaction. Additionally, the formation free energy of the *OCCO intermediate was evaluated under electrochemical conditions.

The screening revealed several promising alloy systems, particularly those involving Pd and Pt alloyed with post-transition metals (PTMs). Notably, Ga-containing alloys such as GaNi and $\mathrm{Ga_2Pt}$ exhibited exceptional stabilisation of the *OCCO intermediate on their (100) facets, suggesting a favourable pathway for C–C coupling. However, they are very succeptible to surface oxidation, hence would necessitate a strategy to avoid the latter.

The ligand effect induced by PTM incorporation was found to lower the d-band center of the transition metal sites, thereby tuning the CO binding strength into the optimal range for eCO_2R. On the TM side, Pd-based alloys exhibit the strongest reaction to PTM ligands among followed by Pt and Ni. Au and Ag could not be activated by alloying.

On the PTM side, Ga, In, Ge, Sn and Bi exhibit a comparably strong effects on the TM substantially reducing $\Delta G_{*\mathrm{CO}}$. Given this strong influence, 1:1 alloys with both Pd and Pt shift $\Delta G_{*\mathrm{CO}}$into the ideal range. Zn and Cd, on the other hand, exhibited a weakened effect on the TM, where 1:1 alloys with Pt are still overbinding CO.

Surface segregation behaviour is highly dependent on the chemical environment; while PTMs tend to surface segregate in vacuum, noble metals dominate the surface under CO-rich conditions. Cd and Hg alloys tend to de-alloy on the surface, while all other PTMs exhibited stable terminations.

Finally, oxidation resistance and HER suppression are governed by the balance between TM and PTM content. Ontop, Sb and Bi showed particular stability against OH-adsorption.

Overall, the identified alloy candidates demonstrate promising activity and stability profiles and we motivate experimental investigation to validate their performance under realistic electrochemical conditions. Possibly, they allow us to finally dethrone Cu as the sole electrocatalyst able to make hydrocarbons from CO_2 in significant amounts.

SUPPORTING INFORMATION

Supplementary information is available online.

AUTHOR CONTRIBUTION

GK - Sole author, original draft, Visualization, Methodology, Investigation, Formal analysis, Data curation, Conceptualization, Software, Validation.

ACKNOWLEDGEMENTS

I am deeply indebted to Karen Chan under who's supervision the data of the presented work has been calculated and discussed. I alo thank Hendrik Heenen for extensive discussions and help in the development of alloy surface sampling routines. Further, I acknowledge discussions and collaboration with Ezra Clark and Brian Seger, who's experimental investigations have been conducted in parallel. Finally, I acknowledge Villum Fonden (grant no. 9455) and Novo Nordisk Fonden (grant no. 0085735) for financial support and the Novo Nordisk Foundation Data Science Research Infrastructure 2022 Grant: A high-performance computing infrastructure for data-driven research on sustainable energy materials, Grant no. NNF22OC0078009.

CONFLICTS OF INTEREST

The authors declare no conflict of interest.

DATA AVAILABILITY STATEMENT

The data supporting this article will be made publicly available at git@github/cattheory/c2screening.git after acceptance of the article.

---

[*] geokast@dtu.dk

[1] P. De Luna, C. Hahn, D. Higgins, S. A. Jaffer, T. F. Jaramillo, E. H. Sargent, *Science* **2019**, *364*, eaav3506.

[2] J. Resasco, A. T. Bell, *Trends in Chemistry* **2020**, *2*, 825.

[3] S. Nitopi, E. Bertheussen, S. B. Scott, X. Liu, A. K. Engstfeld, S. Horch, B. Seger, I. E. L. Stephens, K. Chan, C. Hahn, J. K. Nørskov, T. F. Jaramillo, I. Chorkendorff, *Chemical Reviews* **2019**, *119*, 7610.

[4] A. Bagger, W. Ju, A. S. Varela, P. Strasser, J. Rossmeisl, *ChemPhysChem* **2017**, *18*, 3266.

[5] Y. Hori, Electrochemical CO2 Reduction on Metal Electrodes, in *Modern Aspects of Electrochemistry*, pages 89–189, Springer New York, New York, NY **2008**.

[6] K. P. Kuhl, E. R. Cave, D. N. Abram, T. F. Jaramillo, *Energy & Environmental Science* **2012**, *5*, 7050.

[7] S. Verma, B. Kim, H. R. M. Jhong, S. Ma, P. J. Kenis, *ChemSusChem* **2016**, *9*, 1972.

[8] H. A. Hansen, C. Shi, A. C. Lausche, A. A. Peterson, J. K. Nørskov, *Physical Chemistry Chemical Physics* **2016**, *18*, 9194.

[9] J. Li, J. Halldin Stenlid, M. T. Tang, H. J. Peng, F. Abild-Pedersen, *Journal of Materials Chemistry A* **2022**, *10*, 16171.

[10] K. Tran, Z. W. Ulissi, *Nature Catalysis* **2018**, *1*, 696.

[11] M. Zhong, K. Tran, Y. Min, C. Wang, Z. Wang, C.-T. Dinh, P. De Luna, Z. Yu, A. S. Rasouli, P. Brodersen, S. Sun, O. Voznyy, C.-S. Tan, M. Askerka, F. Che, M. Liu, A. Seifitokaldani, Y. Pang, S.-C. Lo, A. Ip, Z. Ulissi, E. H. Sargent, *Nature* **2020**, *581*, 178.

[12] O. Christensen, S. Zhao, Z. Sun, A. Bagger, J. V. Lauritsen, S. U. Pedersen, K. Daasbjerg, J. Rossmeisl, *ACS Catalysis* **2022**, *12*, 15737.

[13] G. Kastlunger, H. H. Heenen, N. Govindarajan, *ACS Catalysis* **2023**, *13*, 5062.

[14] G. Kastlunger, L. Wang, N. Govindarajan, H. H. Heenen, S. Ringe, T. Jaramillo, C. Hahn, K. Chan, *ACS Catalysis* **2022**, *12*, 4344.

[15] W. Deng, P. Zhang, B. Seger, J. Gong, *Nature Communications* **2022**, *13*, 803.

[16] B. Seger, G. Kastlunger, A. Bagger, S. B. Scott, *ACS Energy Letters* **2025**, *10*, 2212.

[17] F. Calle-Vallejo, M. T. M. Koper, *Angewandte Chemie International Edition* **2013**, *52*, 7282.

[18] R. B. Sandberg, J. H. Montoya, K. Chan, J. K. Nørskov, *Surface Science* **2016**, *654*, 56.

[19] A. Bagger, L. Arnarson, M. H. Hansen, E. Spohr, J. Rossmeisl, *Journal of the American Chemical Society* **2019**, *141*, 1506.

[20] W. Wang, M. Salomone, M. Re Fiorentin, F. Risplendi, G. Cicero, *ACS Electrochemistry* **2025**, *1*, 2512.

[21] M. K. Horton, P. Huck, R. X. Yang, J. M. Munro, S. Dwaraknath, A. M. Ganose, R. S. Kingsbury, M. Wen, J. X. Shen, T. S. Mathis, A. D. Kaplan, K. Berket, J. Riebesell, J. George, A. S. Rosen, E. W. C. Spotte-Smith, M. J. McDermott,

O. A. Cohen, A. Dunn, M. C. Kuner, G.-M. Rignanese, G. Petretto, D. Waroquiers, S. M. Griffin, J. B. Neaton, D. C. Chrzan, M. Asta, G. Hautier, S. Cholia, G. Ceder, S. P. Ong, A. Jain, K. A. Persson, *Nature Materials* **2025**, *24*, 1522.

[22] J. R. Boes, O. Mamun, K. Winther, T. Bligaard, *The Journal of Physical Chemistry A* **2019**, *123*, 2281.

[23] R. Tran, Z. Xu, B. Radhakrishnan, D. Winston, W. Sun, K. A. Persson, S. P. Ong, *Scientific Data* **2016**, *3*, 160080.

[24] J. K. Nørskov, T. Bligaard, A. Logadottir, J. R. Kitchin, J. G. Chen, S. Pandelov, U. Stimming, *Journal of The Electrochemical Society* **2005**, *152*, J23.

[25] K. Mathew, R. Sundararaman, K. Letchworth-Weaver, T. A. Arias, R. G. Hennig, *The Journal of Chemical Physics* **2014**, *140*, 84106.

[26] Y. Hori, R. Takahashi, Y. Yoshinami, A. Murata, *J. Phys. Chem. B* **1997**, *101*, 7075.

[27] C. Chen, Y. Li, S. Yu, S. Louisia, J. Jin, M. Li, M. B. Ross, P. Yang, *Joule* **2020**, *4*, 1688.

[28] R. Tran, Z. Xu, B. Radhakrishnan, D. Winston, W. Sun, K. A. Persson, S. P. Ong, *Scientific Data* **2016**, *3*, 160080.

[29] D. A. Torelli, S. A. Francis, J. C. Crompton, A. Javier, J. R. Thompson, B. S. Brunschwig, M. P. Soriaga, N. S. Lewis, *ACS Catalysis* **2016**, *6*, 2100.

[30] C. W. Li, M. W. Kanan, *J. Am. Chem. Soc* **2012**, *134*, 7231.

[31] E. L. Clark, R. Nielsen, J. E. Sørensen, J. L. Needham, B. Seger, I. Chorkendorff, *ACS Energy Letters* **2023**, *8*, 4414.

[32] D. Hochfilzer, J. E. Sørensen, E. L. Clark, S. B. Scott, I. Chorkendorff, J. Kibsgaard, *ACS Energy Letters* **2021**, *6*, 1879.

[33] S. Vijay, G. Kastlunger, K. Chan, J. K. Nørskov, *The Journal of Chemical Physics* **2022**, *156*.